

# 超音速等离子喷涂层的组织及性能分析

王海斗<sup>1</sup>, 徐滨士<sup>1</sup>, 姜 祎<sup>1,2</sup>, 刘 明<sup>1</sup>, 孙明喜<sup>2</sup>

(1. 装甲兵工程学院 装备再制造技术国防科技重点实验室, 北京 100072; 2. 海军飞行学院, 葫芦岛 125101)

摘要: 用超音速等离子喷涂技术制备了 NiCrBSi 涂层, 并对涂层的组织性能进行了综合分析. 用扫描电镜和能谱仪分析了涂层的内部组织, 用纳米压痕法测试了硬度和弹性模量, 用拉伸试验法测试了涂层与基体的结合强度, 用 X 射线应力仪测定了涂层沿厚度方向的残余应力的分布. 结果表明, 涂层内部比较均匀, 具有较低的孔隙率和氧化物含量. 涂层的纳米显微硬度达到 15 GPa, 纳米弹性模量达到 200 GPa, 涂层与基体的结合强度接近 50 MPa, 涂层具有很好的耐磨性和优异的力学性能. 涂层内部分布着拉应力状态的残余应力, 其随着距离涂层顶部距离的增加而逐渐降低.

关键词: 超音速等离子喷涂; 残余应力; 微观组织; 力学性能

中图分类号: TG 156.99 文献标识码: A 文章编号: 0253-360X(2011)09-0001-04



王海斗

## 0 序 言

热喷涂是指将熔融状态的喷涂材料, 通过高速气流使其雾化喷射在零件表面, 形成喷涂层的一种金属表面加工方法, 具有工艺灵活、适应范围广, 基体及喷涂材料广泛, 生产效率高特点, 已经在航空航天领域得到了广泛的应用<sup>[1]</sup>. 其中, 等离子喷涂的生产效率高、涂层质量好, 在热喷涂行业中始终占据着主导地位, 应用范围非常广泛. 超音速等离子喷涂利用非转移型等离子弧与高速气流混合时出现的“扩展弧”, 从而得到稳定聚集的超音速等离子焰流并进行喷涂的一种方法, 其具有焰流温度高、粒子飞行速度快的优点, 喷涂质量较之普通等离子喷涂技术有明显提高<sup>[2]</sup>. 喷涂层与基体的结合以及涂层内部的残余应力, 对涂层的使用性能有着十分重要的影响. 文中利用超音速等离子喷涂技术制备了镍基超音速等离子喷涂层, 并对其组织及力学性能进行分析, 考察了残余应力在涂层的分布以及对涂层力学性能的影响.

## 1 试验方法

采用装备再制造技术国防科技重点实验室自行

研制的低功率、小气体流量的高效能超音速等离子喷涂系统(HEPJet)制备涂层. 采用超音速喷枪取代了传统喷枪, 对等离子焰流进行压缩, 使其电弧电压高达 200~400 V, 焰流速度超过 3 600 m/s, 粒子飞行速度达到 450 m/s.

采用常用的 NiCrBSi 粉末作为喷涂材料, 其成分如表 1 所示.

表 1 NiCrBSi 粉末的化学成分(质量分数, %)  
Table 1 Chemical composition of NiCrBSi powder

C	B	Si	Cr	Fe	Co	Ni
0.6~1.0	2.5~4.5	3.0~5.0	14~17	≤15	—	余量

喷涂颗粒的形貌几乎都为圆形, 直径都在 100 μm 以下, 如图 1 所示.

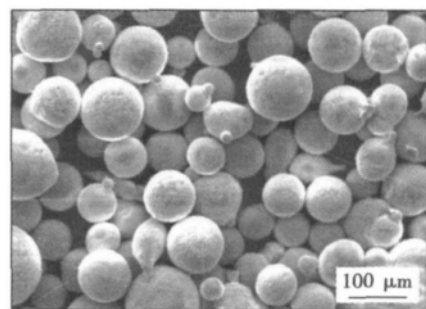


图 1 NiCrBSi 喷涂颗粒形貌  
Fig. 1 Morphology of NiCrBSi powder

收稿日期: 2010-07-09

基金项目: 国家自然科学基金重点资助项目(50735006); 国家自然科学基金面上项目(50675223); 国家 973 计划资助项目(2007CB607601); 国家科技支撑计划资助项目(2008BAK42B03)

为改善结合性能,喷涂时采用 Ni-Al 粉末作为打底层. 喷涂所用的基材材料为调制处理的 45 钢板材,尺寸为 65 mm × 10 mm × 6 mm. 喷涂之前,基材采用丙酮清洗,并预热至 100 ~ 200 °C,然后采用棕刚玉喷砂,提高涂层的结合强度. 为便于喷涂过程的冷却,制备了专用的不锈钢喷涂夹具,并规划了喷涂路径和喷涂参数. 喷砂和喷涂过程中,基材采用夹具固定在不锈钢圆筒上,圆筒外径为 200 mm,厚度为 4 mm. 在喷涂过程中,圆筒的转速为 120 r/min,喷枪垂直于圆筒,并以 12 mm/s 的恒定速度移动,喷涂距离约为 100 mm.

涂层微观形貌及组织的观察采用 Quanta200 型扫描电子显微镜(SEM),化学成分采用同 SEM 配套使用的 Genesis 60s 能谱仪(EDS).

对于涂层的力学性能,首先采用拉伸试验法测量了涂层的结合强度. 使用的胶粘剂为 E-7 胶,其中两组分重量比为 10:1.2. 胶结过程中严格控制对偶试件轴线同轴度. 胶结后保持温度为 100 °C 在烤箱内停留约 3 h 后随炉冷却,放置 24 h 后即可测试. 拉伸试验在 WE-400 型液压万能试验机上进行.

采用 Nano Test 600 型多功能纳米材料性能测试仪测试了涂层的弹性模量,压头为金刚石制成的正三棱锥形 Berkovich 压头,加载载荷为 30 mN,保荷时间为 15 s,随机选取 6 个点进行压痕测试.

采用 X-350A 型 X 射线应力测定仪测试涂层残余应力,该设备采用标准为 GB7704—87 《X 射线应力测定方法》,对于涂层厚度方向,采用电解抛光的方法逐层进行测试. 电解抛光液选择饱和氯化铵溶液 + 3% 甘油(体积比),抛光前首先确定抛光时间、电流和电压等参数下的单道抛光深度,每道抛光深度 20 μm. 并按照该参数进行逐层抛光. 在接近涂层—基体界面时,适当降低电流,通过实时观察以确保腐蚀到基体的表面.

## 2 试验结果与分析

### 2.1 涂层的微观结构及成分分析

从图 2 可以看出,NiCrBSi 涂层的组织结构致密,孔隙率较低,但是内部仍存在少量的孔隙和夹杂. 大气等离子喷涂在制备金属或者金属陶瓷涂层的时候,在层状结构的界面区域存在少量的氧化物条带,影响着层状结构之间的结合强度. 而氧化物的含量与喷涂工艺尤其是颗粒的温度有关. Sampath 等人<sup>[3]</sup>的试验结果表明,随着喷涂颗粒温度的提高,层状结构表面出现氧化现象,涂层内部氧化物含量上升. 其研究表明,涂层内部的孔隙率随着喷

涂熔滴获得的热能的增加而降低,然而涂层内部的氧化物含量却随之增加. 文中对涂层内部的黑色夹杂区域进行能谱分析,如图 3 所示,发现涂层内部确实存在一定的 O 元素,但是含量并不高. 分析原因,喷涂焰流并未经过超音速喷枪的压缩,造成喷涂粒子轰击工件的能量高于普通等离子喷涂系统的焰流. 因此,尽管超音速等离子喷涂功率相对较低,但其焰流经过超音速喷枪的压缩而具有较高的温度和能量,既保证了粉末的充分熔化,熔滴又具有较高的冲击能量. 因此,涂层的孔隙率很低,同时氧化物含量又得到了很好的控制.

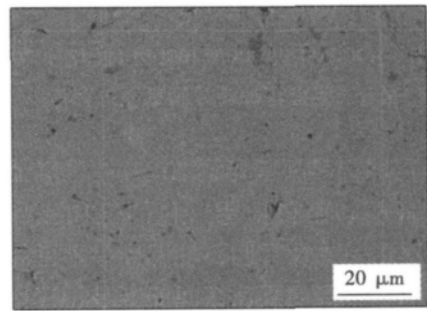


图 2 NiCrBSi 涂层截面组织形貌

Fig. 2 Cross-section morphology of NiCrBSi coating

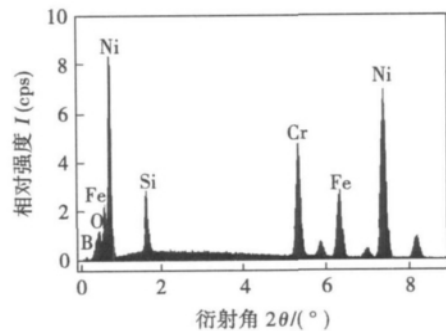


图 3 NiCrBSi 涂层能谱分析

Fig. 3 Energy spectrum of NiCrBSi coating

### 2.2 涂层的微观力学性能

试样的弹性模量根据卸载曲线的斜率测定<sup>[4]</sup>,即

$$E_r = \frac{dF}{dh} \frac{\sqrt{\pi}}{2\sqrt{A}} \quad (1)$$

式中:  $E_r$  为当量折合弹性模量;  $A$  为接触面积;  $\frac{dF}{dh}$  为最大载荷下的卸载刚度. 之后,通过当量弹性模量公式换算出涂层的纳米弹性模量,即

$$\frac{1}{E_r} = \frac{1 - \nu_s^2}{E_s} + \frac{1 - \nu_i^2}{E_i} \quad (2)$$

式中:  $\nu$  为泊松比,角标  $s$  和  $i$  分别代表被测试件和压头. 压头的弹性模量为 1 141 GPa,泊松比为 0.07,涂层试样的泊松比设为 0.31.

涂层纳米硬度  $H_n$  可以根据最大载荷  $P_{max}$  与接触面积  $A$  的关系表征,即

$$H_n = P_{max} / A \quad (3)$$

测试的载荷—深度曲线如图 4 所示,根据上述公式可以换算得出涂层的纳米弹性模量为 200.22 GPa,而纳米硬度为 14.80 GPa. 可以判断,涂层的硬度和弹性模量较高,具有很好的耐磨等力学性能. 同时也发现,尽管在个别测试点上结果具有一定差别,但是大部分测试点的力学性能基本一致,说明涂层内部的力学性能比较均匀.

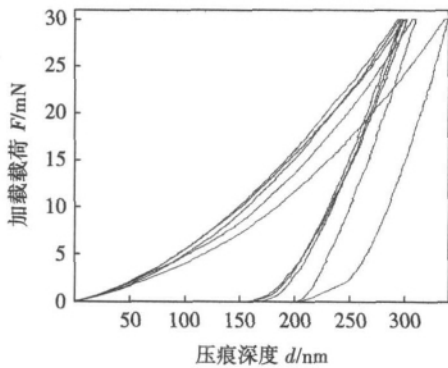


图 4 纳米压痕测试载荷—深度关系曲线

Fig. 4 Load-depth curve of nano indentation test of NiCrBSi coating

### 2.3 涂层的抗拉强度测试

测试结果如表 2 所示,涂层结合强度 ( $R_{bond}$ ) 最高为 50 MPa,基本满足实际工况的需要. 从断口情况来看,断裂部位均在涂层与基体之间,进一步说明涂层内部较为致密,具有较高的内聚强度和力学性能. 但也说明涂层与基体之间的结合仍然以力学结合为主. 涂层与基体之间较低的结合强度会削弱涂层的力学性能和服役性能,但是 NiCrBSi 超音速等离子喷涂层的结合强度接近 50 MPa,可以满足很多

表 2 涂层拉伸结合强度测试结果

Table 2 Bonding strength test of NiCrBSi coating

序号	结合强度 $R_{bond}$ /MPa	拉断部位
1	44	涂层与基体之间
2	50	涂层与基体之间
3	46	涂层与基体之间
4	43	涂层与基体之间
5	48	涂层与基体之间
平均值	46.2	

实际工况的使用要求. 如果采取一些后处理工艺如激光重熔等来提高涂层的内聚强度和力学性能,将会进一步提高涂层的使用性能.

### 2.4 涂层的残余应力测试

等离子喷涂层的厚度一般在 500  $\mu\text{m}$  以下,不同工况下对涂层的厚度要求也不尽相同. 张显程<sup>[5]</sup>在对厚度接近 100  $\mu\text{m}$  的 NiCrBSi 超音速等离子喷涂层的接触疲劳分析中发现,不同载荷条件下涂层的失效形式不同,接触应力较低时涂层以磨损和剥落为主,接触应力较高时以分层失效为主. 为了研究残余应力对涂层内部分层失效的影响,制备的喷涂层厚度为 200  $\mu\text{m}$ ,其中打底层厚度约为 20  $\mu\text{m}$ ,测试结果如图 5 所示. 可以看出,涂层内部的残余应力状态为拉应力,并随距离涂层顶部距离的增加而减少,应力最高值大约在 80 MPa 左右.

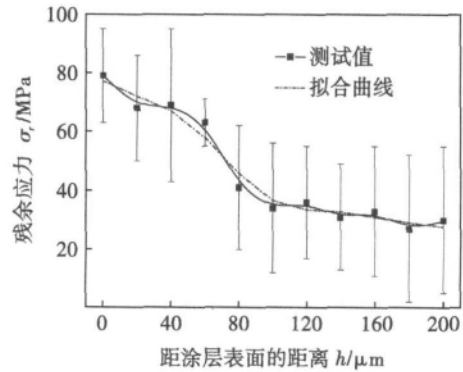


图 5 涂层残余应力沿厚度方向的分布

Fig. 5 Residual stress of NiCrBSi coating along thickness direction

涂层内部的残余应力的产生有三个来源. (1) 熔滴到达基体或者已经凝固熔滴表面时,快速凝固导致的骤冷应力 (quenching stress); (2) 喷涂结束时,涂层和基体共同冷却至室温导致的热应力 (thermal stress); (3) 温度变化时,相变等引起的内应力 (intrinsic stress)<sup>[6,7]</sup>. 对于等离子喷涂的镍基涂层,由相变等因素引起的残余应力对最终涂层残余应力影响很小.

对于单层涂层的热应力解可近似表示为

$$\sigma_{th} = E_c (\alpha_s - \alpha_c) \Delta T \quad (4)$$

式中:  $E_c$  为涂层的弹性模量;  $\alpha_c$  和  $\alpha_s$  分别为涂层和基体的线膨胀系数;  $\Delta T$  为温度差值,因为是冷却过程,所以  $\Delta T$  为负值. 可见,当  $\alpha_c > \alpha_s$  时,涂层产生拉应力状态的热应力;当  $\alpha_c < \alpha_s$  时,涂层产生压应力. 而骤冷应力是单个喷涂颗粒快速冷却区到基体温度的收缩产生的应力,并在收缩过程中颗粒始终受到基体的约束,因此,骤冷应力  $\sigma_q$  始终为拉应

力<sup>[8]</sup>. 图 6 为不同材质的涂层残余应力  $\sigma_r$  的产生示意图<sup>[9]</sup>, 其中  $T_0$  为室温,  $T_s$  为基体温度. 对于 NiCrBSi 涂层来说, 在不同温度下涂层的线膨胀系数均大于基体, 即  $\alpha_c > \alpha_s$ , 属于图 6b 的类型, 因此, 涂层的残余应力最终显示为拉应力.

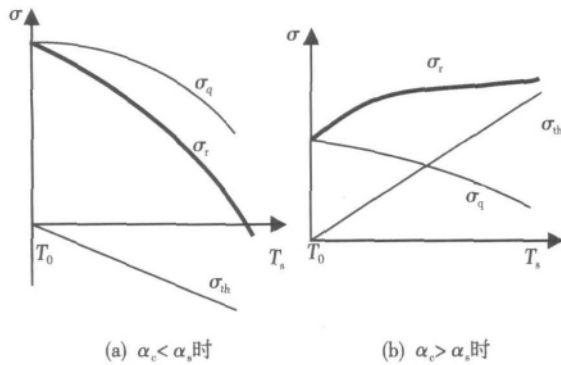


图 6 不同基体温度下的涂层残余应力

Fig. 6 Coating residual stress at different  $T_s$

图 6b 显示随着基体温度的降低, 涂层的残余应力应略有提高. 喷涂中随着喷涂厚度的增加, 相对于新涂层的“基体”的温度也逐渐升高, 残余应力应该随距离表面的增加而增大, 然而实测的残余应力沿厚度分布却呈逐渐下降的趋势. 这主要是由于实际喷涂过程中, 骤冷应力和热应力在喷涂过程中会在涂层和基体中产生不同的应力状态, 并在工件中产生弯矩. 由于弯矩应力的作用, 造成涂层(大部分处于弯矩中性轴上方)内部的应力随着距中性轴距离的增加而增加. 因此, 涂层顶部的残余应力最大.

### 3 结 论

(1) 利用超音速等离子喷涂技术制备 NiCrBSi 耐磨涂层, 微观组织及成分分析表明, 涂层具有较低的孔隙率和氧化物含量.

(2) 对涂层的力学性能分析发现, 涂层具有较高的纳米硬度和弹性模量, 具有很好的耐磨性; 涂层与基体结合强度接近 50 MPa, 且涂层内部较为致

密, 其力学性能比较均匀.

(3) 涂层内部分布着拉应力状态的残余应力, 并随着距离涂层表面距离的增加而逐渐降低, 这是由于涂层残余应力主要来源于热应力和骤冷应力, 两者共同的作用以及在工件内部产生的弯矩决定了涂层内部残余应力的分布.

### 参考文献:

- [1] 张平. 热喷涂材料[M]. 北京: 国防工业出版社, 2006.
- [2] 王海军, 朱胜, 郭永明, 等. 高效能超音速等离子喷涂系统及其应用[J]. 金属加工, 2008(18): 38-42.  
Wang Haijun, Zhu Sheng, Guo Yongming, et al. High-efficiency supersonic plasma spraying system and its application[J]. Metal Forming, 2008(18): 38-42.
- [3] Sampath S, Jiang X, Kulkarni A, et al. Development of process maps for plasma spray: case study for molybdenum[J]. Materials Science and Engineering, 2003, A348(1-2): 54-66.
- [4] Wang Hongmei, Liu Cunlong, Shi Peiing, et al. Design and micro-mechanical properties of nano-SiO<sub>2</sub> strengthened composite coatings towards remanufacturing[J]. Journal of Central South University of Technology, 2005, 12(S2): 190-194.
- [5] 张显程. 面向再制造寿命预测的等离子喷涂涂层结构完整性研究[D]. 上海交通大学博士学位论文, 2007.
- [6] Jiang Yi, Xu Binshi, Wang Haidou. Residual stresses within sprayed coatings[J]. Journal of Central South University of Technology, 2005, 12(S2): 53-58.
- [7] Zhang Xiancheng, Xu Binshi, Wang Haidou, et al. Thermo-mechanical integrity of coatings with residual stresses[C]// Proceedings of the Fracture Mechanics Symposium, Hangzhou: Zhejiang University of Technology Press, 2004: 225-239.
- [8] 姜祚, 徐滨士, 王海斗. 热喷涂涂层残余应力的来源及其失效形式[J]. 金属热处理, 2007, 32(1): 29-31.  
Jiang Yi, Xu Binshi, Wang Haidou. Sources and failure modes of residual stresses in thermal sprayed coatings[J]. Heat Treatment of Metals, 2007, 32(1): 29-31.
- [9] Kuroda S, Clyne T W. Quenching stress in thermally sprayed coatings[J]. Thin Solid Films, 1991, 200(1): 49-66.

作者简介: 王海斗, 男, 1969 年出生, 博士, 教授. 主要从事再制造工程和摩擦学研究. 发表论文 150 余篇. Email: wanghaidou@tsinghua.org.cn.

## MAIN TOPICS ,ABSTRACTS & KEY WORDS

### Microstructure and mechanical properties of supersonic plasma sprayed coating

WANG Haidou<sup>1</sup>, XU Binshi<sup>1</sup>, JIANG Yi<sup>1,2</sup>, LIU Ming<sup>1</sup>, SUN Mingxi<sup>2</sup> ( 1. Science and Technology on Remanufacturing Laboratory, Academy of Armored Forces Engineering, Beijing 100072, China; 2. Naval Flying Academy of China, Huludao 125101, China; ) . p 1 - 4

**Abstract:** NiCrBSi coating was sprayed by supersonic plasma spraying technology, and microstructure and mechanical properties of NiCrBSi coating were analyzed. Microstructure of coating was investigated by scanning electron microscopy (SEM) and energy dispersive spectroscopy (EDS), hardness and elastic modulus were measured by nano-indentation method. Bonding strength between coating and substrate was investigated by tensile test. The distribution of residual stress alongside the coating thickness was measured by X-ray diffraction method. The results showed that the coating structures were uniform and had a low porosity and oxide. Nano-hardness was near to 15 GPa, nano-elastic modulus was 200 GPa and bonding strength was close to 50 MPa. It is concluded that the coating has good wear-resistance and excellent mechanical properties. Residual stress in the coating is tensile, and decreases with the increase of the distance from the coating surface.

**Key words:** supersonic plasma spray; residual stress; microstructure; mechanical properties

### Development of microstructure influence on mechanical properties of fusion welding joints of aluminium alloy 2A12

QIAO Jisen, YU Jiangrui, GOU Ningnian, YUAN Xiaoyu ( School of Material Science and Engineering, Lanzhou University of Technology, State Key Laboratory of Gansu New Non-ferrous Metal Materials, Lanzhou 730050, China) . p 5 - 8

**Abstract:** TIG welding has been carried out for thin plate of aluminium alloy 2A12, and the correlation between microstructure and mechanical properties was analyzed. Coarse and mixed grains were observed in welding area by means of metallographical analysis. From the edge to the center of welding seam, the volume grains changed to isometric grains, a mixed grain distribution was shown near the fusion line. Inhomogeneous mechanical behavior was studied by micro hardness and tensile testing. The results showed that minimal hardness was located in the fusion line, and fracture was also happened in the same area, which was accordance to the microstructure distribution. SEM and electron probe tests were done for fracture analysis and elements identification of welded joints, it was shown that the main reason for strength decreasing of aluminium alloy welded joint was the precipitation phases  $\theta$  and  $s$ , which were generated during cooling process of welding.

**Key words:** welding point; microstructure; mechanical properties; eutectic point

### Investigation preparation method and soldering behaviors of Sn-58Bi lead-free solder with carbon nanotubes

HE Peng<sup>1</sup>, AN Jing<sup>2</sup>, MA Xin<sup>3</sup>, CHEN Sheng<sup>3</sup>, QIAN Yiyu<sup>2</sup>, LIN

Tiesong<sup>1</sup> ( 1. State Key Lab of Advanced Welding Production Technology, Harbin Institute of Technology, Harbin 150001, China; 2. Shenzhen Graduate School, Harbin Institute of Technology, Shenzhen 518055, China; 3. Yik Shing Tat Industrial Co., Ltd, Shenzhen 518101, China) . p 9 - 12

**Abstract:** Varying weight fraction of multi-walled carbon nanotubes were incorporated into Sn-58Bi solder alloy by ball-milling and low temperature melting methods, the morphologies of carbon nanotubes in solder alloy and the influences of carbon nanotubes on the pull-off strength were investigated by SEM, EDS, and DSC. The experimental results indicate that part of carbon nanotubes are incorporated into Sn-58Bi solder alloy after ball-milling and low temperature melting; 0.03% CNTs can improve the wettability; the melting point of Sn-58Bi-CNTs solder does not change much; the dispersive distribution of carbon nanotubes could refine the microstructure of Sn-58Bi-CNTs joints and the reliability of solder joints also is improved by the influences of CNTs on the fracture mechanism of solder joints.

**Key words:** carbon nanotubes; Sn-58Bi solder; ball-milling; low temperature melting

### Analysis of molten pool configuration and welding stability during high-power fiber laser welding

GAO Xiangdong<sup>1</sup>, ZHANG Yong<sup>1</sup>, YOU Deyong<sup>1</sup>, Katayama Seiji<sup>2</sup> ( 1. Faculty of Mechanical and Electrical Engineering, Guangdong University of Technology, Guangzhou 510006, China; 2. Joining and Welding Research Institute, Osaka University, Osaka 567-0047, Japan) . p 13 - 16

**Abstract:** During high-power fiber laser welding, the emission of a molten pool includes plenty of information about welding quality. The configuration and characteristics of a molten pool are related to the stability of welding process. An approach based upon infrared image processing was proposed to analyze the configuration of a molten pool and evaluate the stability of welding process for high-power fiber laser welding. In laser butt-joint welding of type 304 austenitic stainless steel plate with a high power 10 kW continuous wave fiber laser, an infrared sensitive high-speed video camera was used to capture the dynamic images of the molten pools. The configurations of a molten pool and a keyhole were analyzed through image processing techniques such as automatic segmentation by dynamic threshold and mathematical morphology to extract the molten pool edge and measure the molten pool width. The molten pool width, keyhole area and keyhole width were defined as the configuration parameters of a molten pool, and the welded seam width was defined as the parameter reflecting the stability of welding process. Therefore, the correlations among these parameters were investigated, and the actual laser welding experimental results showed that the stability of a high power fiber laser welding process could be monitored and estimated by the defined configuration parameters of the molten pools.

**Key words:** high-power fiber laser welding; infrared image; molten pool; stability